Journal of Catalysis 355 (2017) 120–130

Contents lists available at ScienceDirect

Journal of Catalysis

journal homepage: www.elsevier.com/locate/jcat

The enhancement of direct amide synthesis reaction rate over TiO_2@SiO_2@$NiFe_2O_4$ magnetic catalysts in the continuous flow under radiofrequency heating

Yawen Liu [a], Nikolay Cherkasov [a], Pengzhao Gao [b], Javier Fernández [a], Martin R. Lees [c], Evgeny V. Rebrov [a,d,*]

[a] School of Engineering, University of Warwick, Coventry CV4 7AL, UK
[b] College of Materials Science and Engineering, Hunan University, Changsha 410082, China
[c] Department of Physics, University of Warwick, Coventry CV4 7AL, UK
[d] Department of Biotechnology and Chemistry, Tver State Technical University, 170026, Nab. A. Nikitina 22, Russia

ARTICLE INFO

Article history:
Received 9 June 2017
Revised 5 September 2017
Accepted 12 September 2017
Available online 5 October 2017

Keywords:
Sol-gel method
Core-shell
Composite magnetic catalysts
Sulfated titania
Amide synthesis
Radiofrequency heating
Induction heating

ABSTRACT

A series of TiO_2@SiO_2@$NiFe_2O_4$ composite magnetic catalyst with a core-double shell structure was synthesized by a sol-gel method. The morphology of the catalysts was studied by XRD, SEM, N_2 physisorption and their magnetic properties were examined with magnetometry, and specific absorption rate measurements. The catalytic activity was determined in a direct amide synthesis reaction between aniline and phenylbutyric acid at 150 °C in a fixed bed flow reactor under radiofrequency heating. The intermediate silica layer of the catalyst increased the porosity of the outer titania layer and the specific absorbance rate of the catalyst. The initial reaction rate increased by 61% as compared to a similar core-shell TiO_2@$NiFe_2O_4$ catalyst showing the detrimental effect of nickel ferrite on titania. The reaction rate was further increased by a factor of 3.5 after a sulfation treatment due to an optimum Lewis acid site strength. The highest specific reaction rate over TiO_2@SiO_2@$NiFe_2O_4$ was observed at a 7.5 wt% sulfate loading which was 2.6 times higher as compared to a mechanical mixture of the same composition. The initial reaction rate decreased by 36% after a period of 55 h on stream. The catalyst activity was restored after a treatment with a H_2O_2 solution.

1. Introduction

Electromagnetic heating is an efficient method for direct heating of a reaction medium providing high product yields and energy efficiency [1]. The short distance between the heating source and the substrate provides an excellent temperature uniformity, fast heating rates and decreased heat losses which are the main problems in conventional heating. There are two main methods for electromagnetic heating: (i) microwave heating operating in the GHz frequency range and (ii) radiofrequency (RF) heating operating in the kHz range [2].

Microwave heating, due to low costs and availability of domestic units, is increasingly used in chemical processes such as the synthesis of organic chemicals and nanomaterials, drug discovery and polymer synthesis [3,4]. The main heating principles are (i) molecular friction caused by molecules alignment in the quickly changing field and (ii) ionic conduction for conductive substances [5]. Microwave heating, however, has several major drawbacks such as very limited penetration depth in polar solvents (in the order of a few cm), difficulties in control of the heating rates [6], limited scalability of the microwave cavities [7,8], and field non-uniformity resulting in hot spots and accelerated catalyst deactivation [9].

Radiofrequency (RF) heating does not suffer from these drawbacks. It provides a much higher penetration depth and utilizes easier scalable hardware such as magnetic materials and induction coils connected to an RF generator [2]. During RF heating, the heat is generated by eddy currents, relaxation loss on the conductive material, as well as by the rotating magnetic domains in the ferromagnetic nanoparticles [10,11]. RF heating is traditionally applied on a large scale to the areas that need high temperatures such as metal tempering and welding, alloy synthesis [12], the formation of carbon [13] and silicon carbide nanocomposites [14]. These applications demonstrate scalability of the method [15]. In the last

* Corresponding author at: School of Engineering, University of Warwick, Coventry CV4 7AL, UK.
E-mail address: E.Rebrov@warwick.ac.uk (E.V. Rebrov).

https://doi.org/10.1016/j.jcat.2017.09.010
0021-9517/

decade, RF heating was applied in catalytic organic synthesis. Kirschning et al. studied several organic reactions in an RF-heated continuous reactor operated at 25 kHz. They reported higher reaction rates as compared to a conventionally-heated reactor due to the direct heat generation in the material [16]. A high product yield of 92% was reported in the condensation reaction to form thiazole over a Pd/silica-coated magnetite catalyst. A reaction rate of up to 4 mmol L^{-1} h^{-1} was reported in the continuous synthesis of neurolepticum olanzapine over a MagSilica300 commercial magnetic catalyst [17]. A gold-functionalized MagSilica300 catalyst was studied in the oxidation of allylic and benzylic alcohols in a flow reactor and showed a close to 100% yield [18].

Under RF heating, the composite magnetic catalyst should provide both high heating and reaction rates. A core-shell structure is often used because the shell layer often acts as a catalyst and protects the magnetic core from chemical erosion and aggregation [19,20]. However, the charge transfer between the core and shell elements is often detrimental for catalytic properties [20,21]. Beydoun et al. [21] observed the photodissolution of the catalytic titania shell at the boundary with the magnetic core which changed the magnetic properties and reduced the catalytic activity. To avoid this detrimental effect, an intermediate silica layer was introduced to prevent the solid state reaction at the interface [22,23].

Following this idea, we developed a series of core-double shell composites with an intermediate silica layer for direct amide synthesis, which is one of the most important reactions in pharmaceutical industry. About 25% of all drugs on the market contain amide bonds, and the amide synthesis covers 65% of drug candidates [24]. Detailed methodologies for the amide formation are presented in several recent reviews [24–27]. In summary, the traditional synthesis involves the activation of carboxylic acids followed by ammonolysis of the activated compound to obtain amide as presented in Fig. 1. The activation step is performed with coupling agents, and the final product is either separated from the reaction mixture or obtained in situ. Typical activating agents involve thionyl chloride ($SOCl_2$), phosphorous oxychloride ($POCl_3$), oxalyl chloride $(COCl)_2$ or a two-step approach of forming a hydrazine derivative followed by nitrous acid treatment [27]. All the compounds are hazardous, result in reactions with very poor atom efficiency (meaning toxic waste) and complicate the synthesis procedure. The direct amide synthesis from carboxylic acids and amines without the activation stage is also possible, however, it is more challenging because it requires high temperature due to low reaction rates and a stable acidic catalyst.

This study follows our previous work [20,28,31] where we developed different titania-containing composite catalysts for this reaction. The main problems with these catalysts were (i) the relatively fast catalyst deactivation due to product inhibition, as a result of a strong product adsorption on the titania surface and (ii) limited reaction rate. A long-term irreversible deactivation was also observed, caused by the interaction of titania with the magnetic core at high temperature required to carry out the reaction.

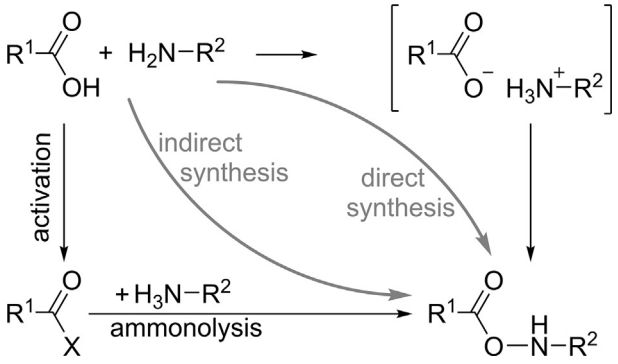

Fig. 1. The general scheme of amide synthesis, adapted from Refs. [24,27].

The limited reaction rates over titania catalysts can be improved by a sulfation treatment as demonstrated by Nagarajan et al. [28] for a range of aromatic acids and amines. The sulfated TiO_2 is an efficient catalyst in the amidation of various acid and amine combinations at 115 °C with the amides yield usually exceeding 95% after a reaction time of 3 h [29]. Chaudhari et al. [30] studied the amide synthesis over acids and sulfated tungstates, and identified that catalytic activity significantly depends on the acid type. Arena et al. [31] showed the following reaction rate sequence is observed TiO_2 (P25) > $ZrO_2 \approx CeO_2$ > γ-Al_2O_3 caused by the chemical and surface properties of the catalysts. To the best of our knowledge however, there is very little systematic studies about the effect of sulfation treatment on the direct amide synthesis reaction rates to allow for efficient catalyst development.

In this study, we investigated the effect of the acid site density and strength over a range of sulfated titania and composite catalysts. In addition, an intermediate silica layer has been introduced in an attempt to suppress the interactions between titania and nickel ferrite to enhance the catalytic activity.

2. Experimental

2.1. Synthesis of composite magnetic catalysts

A nickel ferrite sol was prepared by redispersion of 3 g of nickel ferrite nanoparticles obtained by a sol-gel method [32] in 285 mL of a 2 M ammonia in a water-ethanol (1:3 v/v) solution under continuous sonication for 2 h followed by the addition of 0.3 g of cetrimonium bromide (CTAB) and aging overnight under continuous stirring. A titania sol (0.48 mol L^{-1} TiO_2) was prepared by dissolving titanium(IV) butoxide (85 mL), diethanolamine (25 mL) in ethanol (285 mL). Then 10 mL of a water-ethanol (1:10 v/v) solution was added dropwise and the mixture obtained was stirred for 48 h.

In the next step, the desired amount of the titania sol was added dropwise to the nickel ferrite sol under stirring and the mixture was aged for 48 h. Then the temperature of the mixture was increased to 40 °C under reflux for 24 h and finally to 60 °C without reflux to evaporate the solvent. The solids obtained were dried at 80 °C to produce as-synthesised TiO_2@$NiFe_2O_4$ (shell@core) catalysts which will be referred to as T2A(n) hereafter, where *n* represents the titania loading in wt%. Some of these T2 A samples were calcined at a desired temperature for 1 h with a heating rate of 1 °C min^{-1}. The calcined catalyst will be referred to as T2(n) hereafter. A scheme of the catalyst synthesis and the corresponding sample codes are shown in Fig. 2. The synthesis methods are described in the Supplementary Material, SM1, in more details.

The synthesis of TiO_2@SiO_2@$NiFe_2O_4$ composite magnetic catalysts started with the preparation of SiO_2@$NiFe_2O_4$ samples. They were prepared by dropwise addition of 12.5 mL the silica sol (0.49 mol L^{-1}; obtained from tetraethyl orthosilicate) to the previously prepared suspension containing $NiFe_2O_4$ nanoparticles. The temperature of the resulting suspension was increased to 40 °C under reflux for 48 h and finally to 60 °C without reflux to fully evaporate the solvent. The powder obtained was dried at 80 °C and then calcined in air at 700 °C for 1 h at a heating rate of 2 °C min^{-1}. The sample will be referred to as Si2 hereafter. In the final step of preparation, the Si2 powder was redispersed in a water-ethanol solution and the desired amount of titania sol was added following the same aging and calcination procedures as described above for the T2 samples. The as-synthesized and calcined samples will be referred to as T3A and T3 respectively.

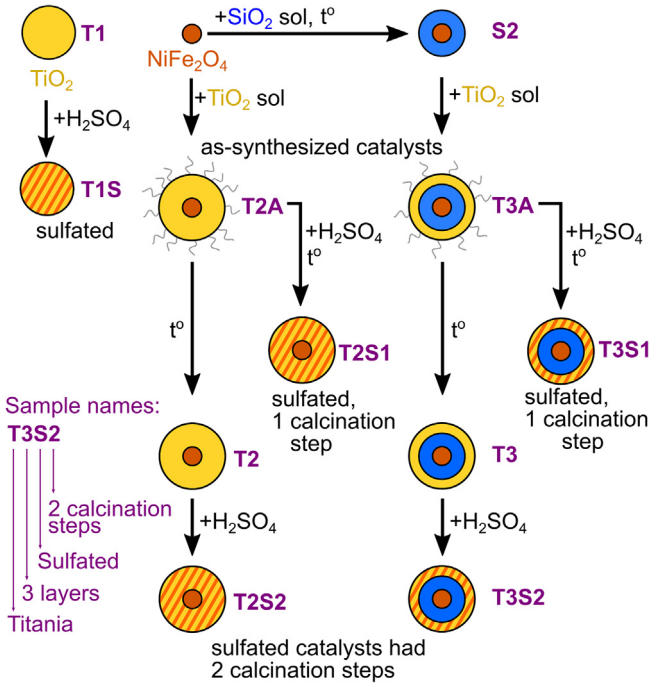

Fig. 2. Scheme of the catalyst synthesis and the corresponding sample codes.

2.2. Sulfation of the catalysts

The T1 (commercial P25 from Sigma Aldrich), T2 or T3 catalysts (1 g) were suspended in 40 mL of a sulfuric acid solution and mixed for 4 h. The extent of sulfation was varied by changing the concentration of the sulfuric acid in the solution. The slurry was then centrifuged, dried and calcined at 500 °C. The sulfated samples are labelled with the index Sx in the sample code, and the number *x* refers to the total number of calcination steps. This number is 1 when the sulfated catalysts were prepared from as-synthesized T2A or T3A samples and the number is equal to 2 when the T2 and T3 samples were used. The nominal loading of sulfate species (in wt%) is shown in brackets in the sample code.

Two reference catalysts have also been prepared. A physical mixture of the T1S and $NiFe_2O_4$ pellets was prepared in a shaker (referred as Mech hereafter). The other reference catalyst was obtained by ball-milling of a mixture of the T1 S catalyst with $NiFe_2O_4$ nanoparticles in an agate jar for 30 min (referred as Ball hereafter).

2.3. Catalyst characterization

Powder X-ray diffraction (XRD) patterns were recorded using a PANalytical Empyrean diffractometer with a Cu Kα radiation at a scanning rate of 2° 2θ min^{-1}. The morphology of the samples was studied with a field emission scanning electron microscope (SEM, Carl Zeiss Sigma). The elemental composition was determined with an energy dispersive spectrometer (EDS) calibrated using the samples with known concentrations of the elements. Prior to analysis, the catalyst samples were not coated with a conductive layer to ensure accurate measurements. The surface chemical composition and electronic state of the elements were analyzed using an X-ray photoelectron spectrometer (XPS, ESCALab250) with a monochromatic 150 W Al Kα radiation. The pass energy for the high-resolution scan was 30 eV and the base pressure of 6.5×10^{-10} mbar. The binding energies were referenced to the C1s line at 284.8 eV.

The magnetic properties of the catalysts were measured by a vibrating sample magnetometer (VSM, Oxford Instruments) in a magnetic field ranging from −5 to 5 kG. The saturation magnetization and coercive field were determined from the hysteresis loop. The specific absorption rate (SAR) was determined by recording the temperature change of a mixture containing catalyst (10 mg in water) placed in the center of a 5-turn coil connected to a radiofrequency generator (Easyheat, 300 kHz, 200 A) [33].

The specific surface area and the total pore volume were determined by nitrogen physisorption at 77 K using a Micromeritics ASAP 2020 porosimeter. Prior to the measurements, the samples were degassed until a residual pressure of 10^{-4} mbar at 250 °C for 1 h was reached.

The identification of the nature of acid sites was performed using pyridine adsorption performed inside an in-situ IR flow cell for a catalyst wafer maintained at a desired temperature. Prior to the experiments, the catalyst was degassed by heating the cell to 150 °C for 30 min under argon flow. The sample was then cooled down to 25 °C and the Ar flow was replaced with a flow of 2.0 vol% pyridine in Ar. After 30 min, the temperature was increased to the desired temperature (40, 100, 150, or 200 °C) and the pyridine mixture cell was replaced with an Ar flow. Then the IR spectrum was recorded with an FTIR spectrometer at a resolution of 2 cm^{-1} (Bruker Vertex 70).

The concentration profiles of CO, CO_2 and H_2O desorbed from the spent catalysts during temperature programmed oxidation (TPO) were recorded using a quadrupole mass spectrometer. In these experiments, the sample (50 mg) was placed in a quartz tube inserted into an oven. A mixture of 20 vol% O_2 and 5 vol% Ar (internal standard) in He was fed over the sample and the temperature was increased at a rate of 5 °C min^{-1}.

Ammonia chemisorption profiles were recorded in the same setup. The catalyst sample (100 mg) was placed in a quartz tube, heated to 400 °C for 30 min under nitrogen flow (20 mL min^{-1} STP prior to the adsorption). The sample was cooled down to 150 °C and adsorption was performed from a mixture containing 1.9 vol% NH_3 and 2.4 vol% Ar (internal standard) in N_2. A blank experiment with the same volume of SiC pellets was performed to subtract the background signal due to ammonia chemisorption onto the gas lines maintained at 110 °C [34].

2.4. Catalytic activity measurements

Two reactor types were used in this study. A continuously stirred tank reactor was used to optimize the catalyst composition. In these experiments, a degassed solution of 4-phenylbutyric acid (50 mM) and aniline (50 mM) in p-xylene and the catalyst pellets (fraction size: 10–40 μm) were loaded into a stainless steel Parr reactor. The temperature was increased and the pressure was set at 10 bar using nitrogen. The absence of external mass-transfer limitations was demonstrated by the constant reaction rate at the stirring rate above 650 rpm. The absence of internal mass transfer limitations was confirmed as the highest Weisz-Prater number in this study was $0.14 \ll 3$ [35].

A glass reactor (Omnifit HiT, i.d 6.6 mm, 250 cm long) was used in flow experiments (Fig. 3). Two HPLC pumps (Shimadzu LC-20ADXR) were used to feed the N_2-degassed solutions of 4-phenylbutyric acid (100 mM) and aniline (100 mM) in p-xylene to the reactor. The initial concentrations were selected such that after the mixing, they would be the same in the batch reactor. The flow reactor was packed with the catalyst pellets (fraction size: 125–250 μm) and it was placed in the center of an 8-turn RF coil operated at 300 kHz. A 5-mm preheating zone was packed with Fe_3O_4 pellets of the same size. A fiber optic temperature sensor (Opsens) was attached to the outer surface of catalytic zone to control the temperature within ±0.1 °C of the set point using a PID con-

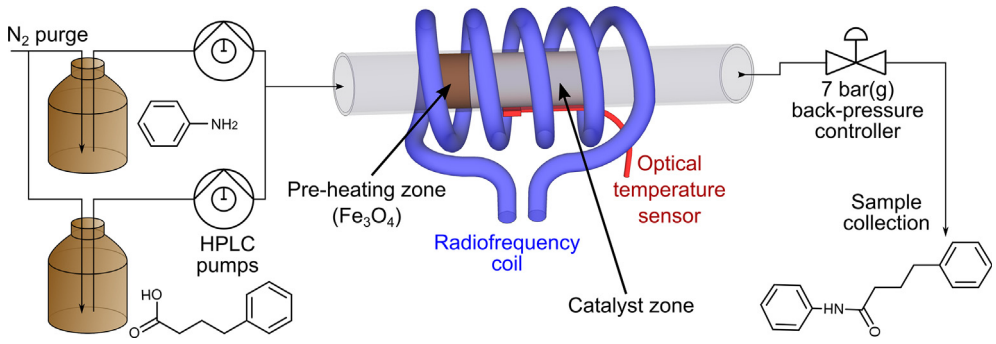

Fig. 3. Scheme of the RF-heated flow reactor used for direct amide synthesis.

troller connected to the RF generator. The reactor was insulated with a 1 cm thick layer of ceramic wool. A total pressure of 7 bar (gauge) was maintained in the reactor with a back pressure controller to keep the reaction mixture in the liquid phase.

The samples were collected at regular time intervals and analyzed by a Shimadzu GC-2010 gas chromatograph (GC) equipped with a FID detector and a 30 m Stabilwax capillary column. Tetradecane was used as internal standard, carbon balance for all the reactions was 99 ± 2%.

The spent catalysts (typically after 2 days on stream) were regenerated in the same flow set-up at 90 °C using a 35 wt% H_2O_2 solution which was fed at a flow rate of 100 μL min^{-1} for 22 h. Before and after the regeneration, the catalysts were flushed with a flow of isopropanol (10 ml total).

3. Results and discussion

3.1. Characterization of composite catalysts

Temperature-programmed oxidation experiments over the T3A catalysts were performed to select the appropriate calcination temperature for the removal of surfactants (Fig. 4). Below 150 °C, only physically adsorbed water is desorbed as indicated by the absence of CO_2 evolution. The main peaks of H_2O and CO_2 are centred at 250 °C. A very high H_2O peak and the C/H ratio of only about 0.02 also suggest a significant removal of strongly adsorbed water from the catalyst pores or dehydration of the adsorbed organic species. The presence of the CO_2 peak indicates oxidation or decomposition of organic species, likely surfactant molecules from the as-synthesised catalyst. At a higher temperature, two smaller CO_2 peaks at 390 and 485 °C observed show a stepwise decomposition of the organic compounds. The increased C/H ratio of 2.0 for the 390 °C peak indicates oxidation of the coke formed by dehydration of the organic compounds. The highest temperature peak had the highest C/H ratio of 2.9 demonstrating a graphitic nature of the coke remaining inside the pores. The presence of graphitic coke is also indirectly confirmed by the high oxidation temperature of 485 °C [36–38]. Importantly, no formation of H_2O and CO_2 occurred above 500 °C, showing that this temperature is sufficient for the full removal of the surfactant from the composite catalysts.

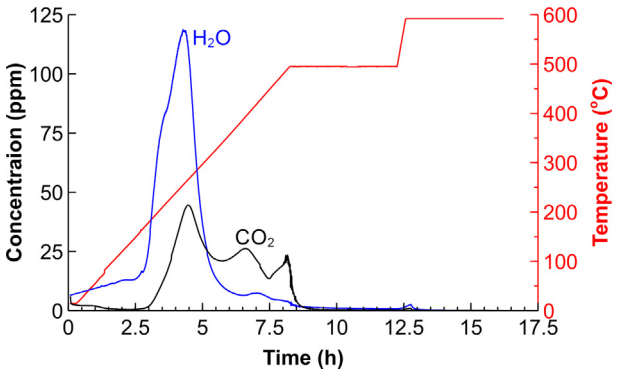

Fig. 4. CO_2 and H_2O concentration profiles (left y-axis) and temperature profile (right y-axis) in a TPO experiment over the T3A catalyst.

To study the effect of calcination time, the as-synthesized T3 A catalyst was calcined at 500 °C for different time intervals. The most dramatic change was observed between 1 and 2 h. The catalyst calcined for 1 h had a surface area of 49 m^2 g^{-1} (Table 1) similar to that of the reference T1 catalyst. However, the surface area decreased to 11 m^2 g^{-1} after calcination for 2 h which was likely caused by the sintering of the porous TiO_2 shell. Therefore for further study, all the samples were calcined for 1 h.

The actual elemental composition of T3(17) (Table 1) was in good agreement with its nominal composition of 11 wt% SiO_2 and 14 wt% TiO_2. These data suggest that the thickness of both titania and silica shells are similar considering their close apparent density. It can also be concluded that the catalyst composition can be controlled by adjusting the initial composition of the corresponding precursors.

The morphology of the T3(17) catalyst was studied with TEM (Fig. 5). The mean size of $NiFe_2O_4$ core was 70 ± 20 nm, which was the same as that in the initial $NiFe_2O_4$ nanoparticles. This indicates the absence of the solid-state reaction between the $NiFe_2O_4$ core and the adjacent silica layer during the calcination steps. The total thickness of the shell layers was 30 ± 10 nm.

Fig. 6 shows XRD patterns of the T2(17) and T3(17) catalysts. The peaks at 25.4 and 48.2° 2θ correspond to the (1 0 1), (2 0 0) crystal planes of anatase (JCPDS card No. 78-2486). The peaks at 30.7, 36.0, 37.6, 43.8, 54.8, and 64.4° 2θ are assigned to the $NiFe_2O_4$ structure (card 74-2081). Minor amounts of α-Fe_2O_3 (card 33-0664) are confirmed by the peaks at 31.4 and 41.3° 2θ. The

Table 1
Physical, magnetic, and catalytic properties of composite catalysts.

Catalyst	T2(17)	T3(17)
$NiFe_2O_4$ content (wt%)	83	70
SiO_2 content (wt%)	0	13
TiO_2 content (wt%)	17	17
BET surface area (m^2 g^{-1})	25	49
Mean core particle size[a] (nm)	51	51
Coercivity (kG)	0.27	0.27
Magnetic saturation (emu g^{-1})	25.0	23.5
Hysteresis area (J g^{-1})	0.43	0.51
SAR[b] (W g^{-1})	1.1	1.5

[a] Estimated by the Scherrer equation.
[b] Specific absorption rate of RF radiation.

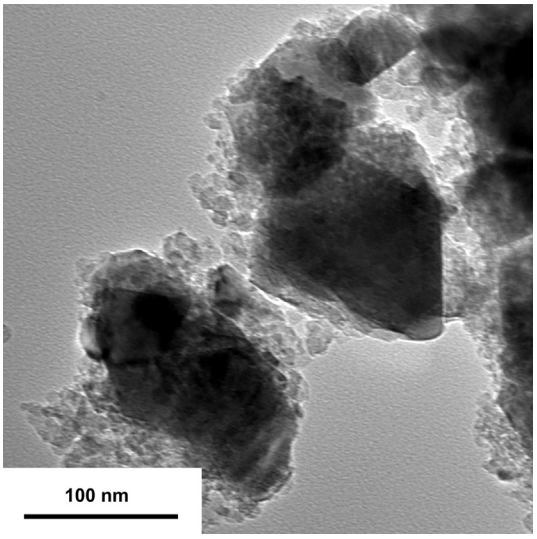

Fig. 5. TEM image of the T3(17) catalyst.

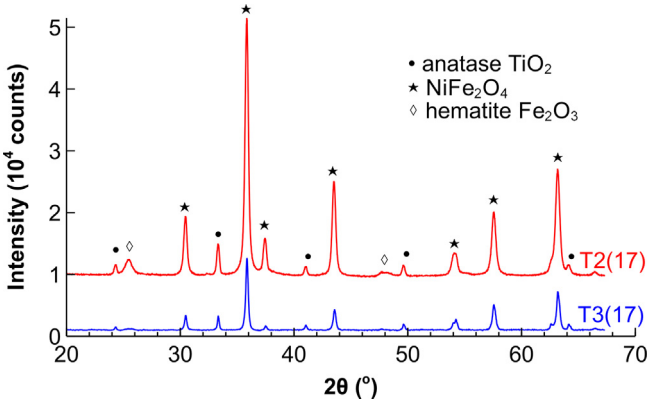

Fig. 6. Powder XRD patterns of the (a) T2(17) and (b) T3(17) catalysts.

α-Fe_2O_3 phase is an impurity usually observed in the low-temperature nickel ferrite synthesis [39]. No SiO_2 peaks are detected in the XRD pattern of T3(17) suggesting its amorphous structure. The mean crystal size of the $NiFe_2O_4$ nanoparticles was found to be the same (51 nm) in both T2(17) and T3(17) catalysts. This size is slightly below the mean size obtained from the TEM images. It appears some agglomeration of nickel ferrite nanoparticles occurs prior to their enclosure by the silica layer. This observation also confirms that the deposition of an outer shell and subsequent chemical and thermal treatments do not change the size of the magnetic core.

Magnetic hysteresis loops of the T2(17) and T3(17) catalysts are shown in Fig. 7. The coercivity was the same for both catalysts as it is mainly determined by the mean particle size of the magnetic core [40], which in turn, was the same in both samples (Table 1). The remnant magnetization was, however, higher for T3(17) compared to T2(17), which is likely explained by the different defect density in the magnetic materials [41–43]. A lower saturation magnetization for T3(17) compared to T2(17) was due to an additional shell present in this sample which increased the total weight of non-magnetic layers (Table 1).

The hysteresis area of T3(17) was higher than that of T2(17) despite the lower saturation magnetization (Table 1). This area is proportional to the energy released per cycle of magnetic field reversal. These data are consistent with the specific absorption rate

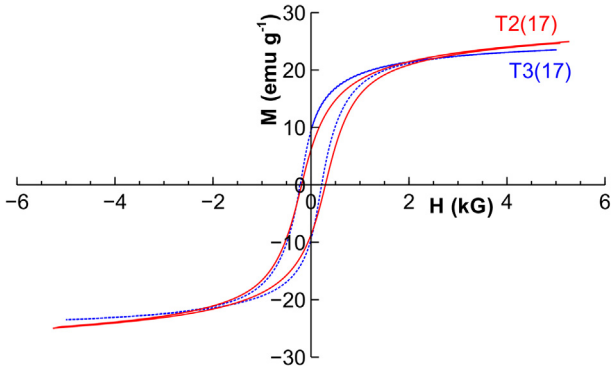

Fig. 7. Magnetisation versus the applied field curves for the T2(17) and T3(17) catalysts.

results which characterize the heating power released per gram of the material being placed under RF field. A similar effect of increased magnetization of silica-encapsulated $CoFe_2O_4$ magnetic nanoparticles was observed by Hutlova et al. [41] caused by an enhanced anisotropy, which was also likely the case for the silica-layered T3 catalyst.

Likely, due to the presence of a chelating ligand (diethanolamine), mesopores with a mean size of 3.0 nm were formed in both catalysts as shown in Fig. 8 [44–46]. Interestingly, both catalysts have a very similar pore size distribution in the mesoporous area. The formation of a mesoporous layer is greatly beneficial to enhance the mass transfer towards the catalytic sites [35].

The T3(17) catalyst has a twofold higher specific surface area and the total pore volume as compared to T2(17) (Table 1). We can assume that the total surface area of the composite catalyst is a linear combination of the areas of the core and the shell (Eq. (1)).

$$A_{total} = x_{shell}A_{shell} + x_{core}A_{core} \quad (1)$$

where x_{shell} and x_{core} are the weight fractions of the shell and the core, A_{shell} and A_{core} are the corresponding specific surface areas, respectively. The assumption is valid if the shell provides complete access for the nitrogen molecules to the core, which seems reasonable in our case considering the low thickness of the shell (Fig. 5) and its high porosity (Fig. 8). The $NiFe_2O_4$ core has a very low area of 2.0 $m^2\ g^{-1}$. From Eq. (1), the specific surface area of the titania shell in the T2(17) and T3(17) catalysts is estimated to be 125 and 136 $m^2\ g^{-1}$, respectively. This result illustrates that the specific surface area of titania shell increases when deposited onto a silica layer rather than directly onto the magnetic core. This is another advantage of the double shell catalysts in addition to the elimina-

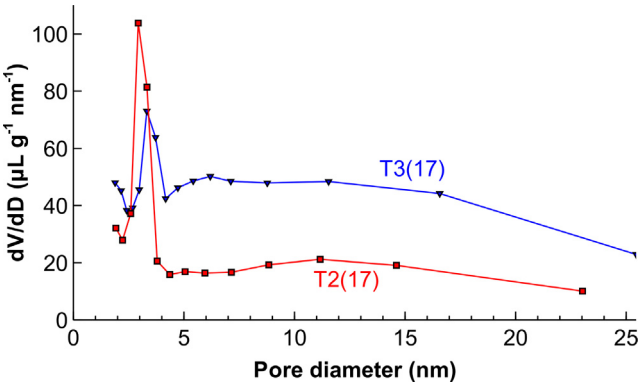

Fig. 8. Pore size distribution for the catalysts studied.

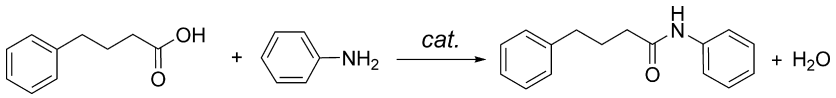

Fig. 9. The scheme of the 4,N-diphenylbutynamide synthesis.

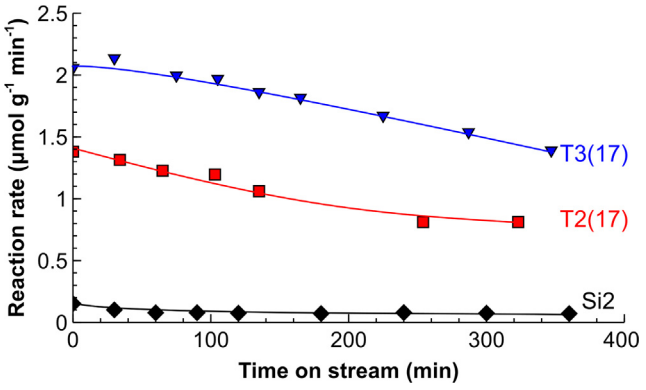

Fig. 10. Direct amide synthesis reaction rates as a function of time on stream over the magnetic composite catalysts at the flow rate of 40 μL min^{-1} (50 mM 4-phenylbutyric acid, 50 mM aniline), 320 mg of the catalyst, 150 °C, 7 bar(g) in the RF-heated reactor.

tion of detrimental core-shell electronic interaction by an intermediate layer [20,21], and its higher SAR values.

The catalytic activity was compared in the reaction between 4-phenylbutyric acid and aniline (Fig. 9). In all the experiments, no products other than the amide were identified and the carbon balance was 99 ± 2%. The reaction kinetics is the first order in respect to both amine and acid and it is controlled by strong product inhibition under the given experimental conditions at conversion levels above 50%. Hence, for proper comparison of the catalysts studied, the conversion was kept below 40% and the results are discussed in terms of the initial reaction rates (see SM2 in the Supplementary Material for details).

The reaction rate over the T3(17) catalyst was 52% higher compared to T2(17) (see Fig. 10). The reference Si2 catalyst showed a negligible activity confirming that the silica layer behaves as an inert material in this reaction. The difference between the catalysts becomes even larger when we compare the rates normalized per available surface area of titania in these catalysts. The reaction rate normalized by surface area over the T3(17) catalyst was larger by 61% compared to T2(17) at the same reaction conditions. Hence, the addition of the SiO_2 layer provides a significant increase in the intrinsic reaction rate over the catalytic sites located onto the titania surface. This is likely caused by the elimination of charge transfer between the nickel ferrite and titania [20,21]. The deactivation rate of T3(17) was also found to be slower than that of T2(17).

3.2. Effect of the sulfation treatment

The electron-withdrawing Lewis acid sites play the main role in the direct amide synthesis over titania catalysts. It is well accepted that the final step of the reaction mechanism includes an attack of the nucleophilic nitrogen atom of the amine towards the carbon atom of the acid forming the amide bond. The electron density on the carbon atom is decreased via an interaction with the carboxylate oxygen atoms [47]. The contribution of the Brønsted acid sites is considerably lower [48].

The direct amide synthesis reaction rate over titania can be increased using a sulfation treatment [28,49]. However, the effect

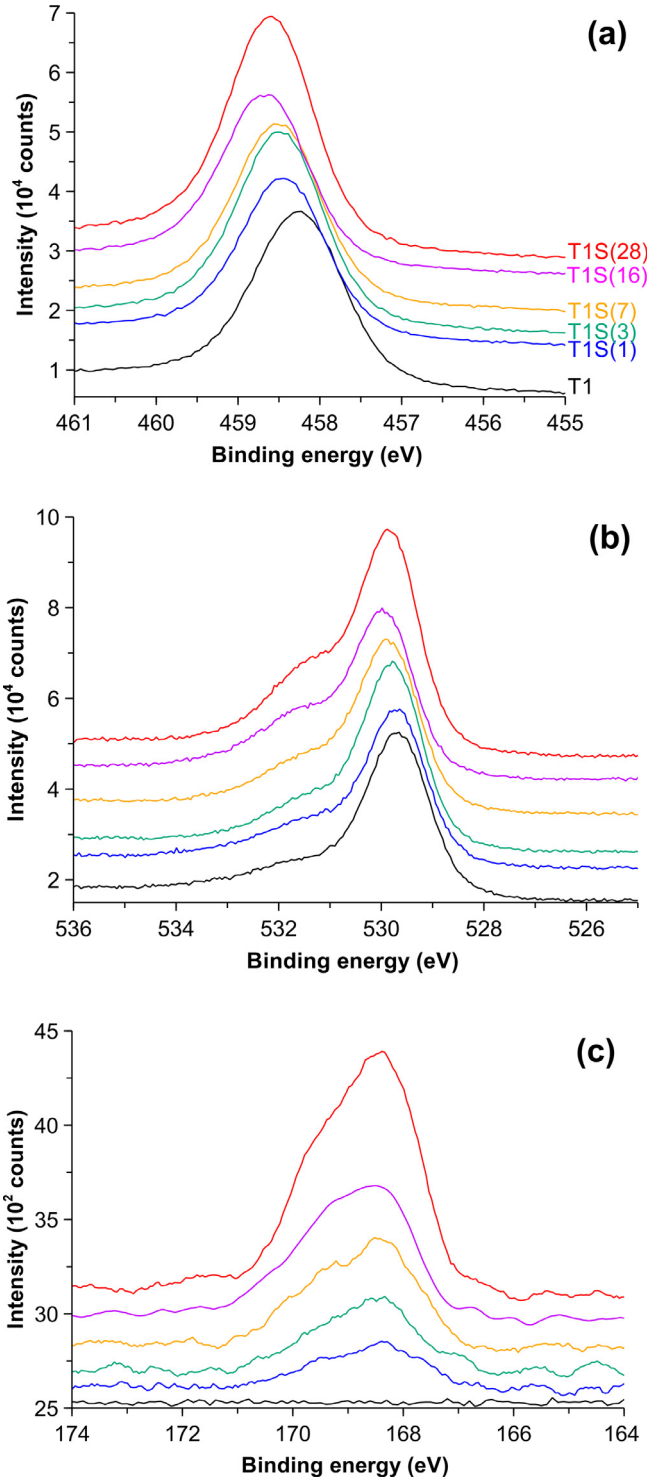

Fig. 11. X-ray photoelectron spectra of the T1S catalysts with various sulfate loading in brackets, (a) Ti 2p$_{3/2}$, (b) O1s, (c) S 2p.

of SO_4^{2-} loading had not been studied in details to the best of our knowledge. Therefore, we prepared a range of sulfated titania samples to obtain the structure-activity relationship between the

amount of SO_4^{2-} species and the catalytic activity. To simplify the analysis and quantification of the data, the T3 catalysts were replaced with the corresponding T1 catalysts with the same titania morphology. The phase composition study showed no change on sulfation as presented in Fig. SM3 of the Supplementary Material.

The Ti $2p_{3/2}$ XPS line in the T1 catalyst is observed at 458.0 eV (Fig. 11a). After sulfation, the peak shifts to higher binding energies due to the electron-withdrawal effect of sulfate groups [50] and associated surface species [51]. The presence of sulfate species also results in the formation of a shoulder in the spectrum of the O 1 s at 531.4 eV next to the main line centered at 529.9 eV (Fig. 11b). Its intensity increases with the concentration of sulfate species. The formation of the shoulder agrees with the XPS studies over sulfated titania catalysts and is attributed to the presence of O-S bonds [52]. The main oxygen line also shifts to higher energy indicating the presence of S-O-Ti bridges [53–55]. The S 2p line is present in all XPS spectra of sulfated samples (Fig. 11c). The binding energy of sulfur in the range from 168.4 to 168.7 eV is characteristic for a hexavalent oxidation state in the SO_4^{2-} species.

The surface sulfur loading determined by XPS versus nominal loading is shown in Fig. 12. It can be seen that the surface sulfur loading is very close to the nominal composition up to a loading of 7.5 wt% suggesting that all sulfur is present near the outer surface of the nanoparticles. This behavior suggests that all the external sites are covered with SO_4^{2-} at a loading of 7.5 wt%. At higher loadings, the sulfur incorporation into the catalysts decreases likely due to a change in the coordination from bridge to chelate [51,56].

The nature of the acid sites on the sulfated catalysts was investigated by IR study of adsorbed pyridine (Fig. 13a). A characteristic Brønsted acid site band at 1540 cm^{-1} [57–59] was not observed in all spectra showing that the sulfated catalysts have no Brønsted acidity. The presence of Lewis acid sites is confirmed by the bands at 1445, 1574, 1604 cm^{-1} and 1490 cm^{-1} [60,61].

The relative strength of the acid sites was studied in the temperature programmed desorption of pyridine (Fig.13a). As the temperature increases, the intensity of all bands decreases due to desorption of pyridine. This method allows to estimate the relative acid strength of different sites while it remains rather qualitative because the band intensity changes with temperature [62,63]. Therefore, the intensity of all bands was normalized to the intensity of the strongest band at 1445 cm^{-1} measured at 40 °C to study the relative acid strength. In the sample with the highest sulfur loading of 28 wt%, the relative intensity was as high as 80% even at 200 °C indicating very strong adsorption of pyridine. Interestingly, the slope of the lines in Fig. 13b decreases as the sulfur loading increases. It shows that both the desorption activation energy

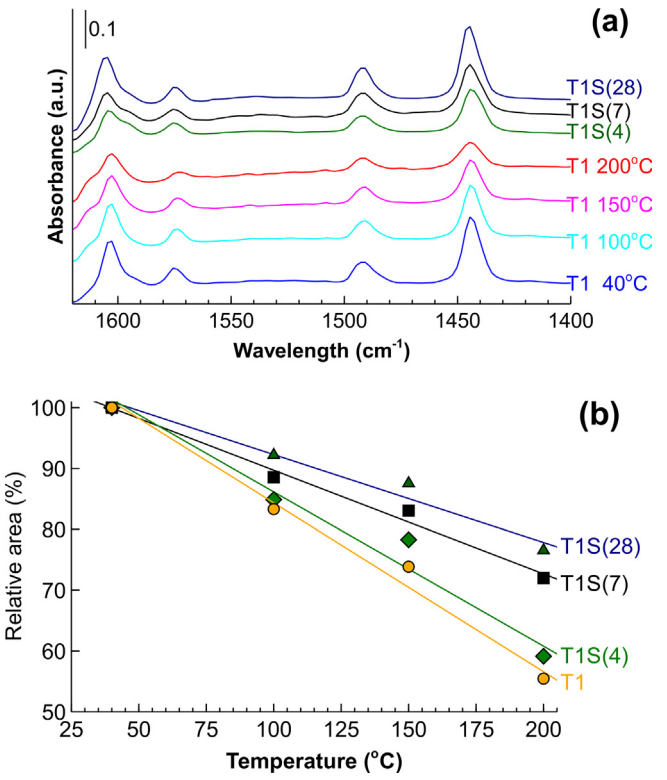

Fig. 13. (a) FTIR spectra of pyridine over sulfated titania catalysts and (b) temperature dependence of the normalized intensity of the 1445 cm^{-1} band at 40 °C.

of pyridine and the strength of Lewis acid sites monotonously increase with sulfur loading.

The total amount of acid sites was studied using ammonia chemisorption from the NH_3 capacity in the adsorption mode at 150 °C. This temperature was chosen to minimize the amount of physically adsorbed ammonia [64]. It should be mentioned that the desorption mode (TPD) could not provide quantitative data because the decomposition of sulfur sites occurs below the temperature of complete ammonia desorption (>450 °C) [58–60]. The results show that the extent of sulfation does not affect the number of acid sites on the surface (Fig. 12). While Wang et al. [65] reported a different dependence, their catalysts had both Brønsted and Lewis acid sites. Therefore, no direct comparison is possible, because the presence of Brønsted acid sites may have altered the adsorption mode of sulfate species.

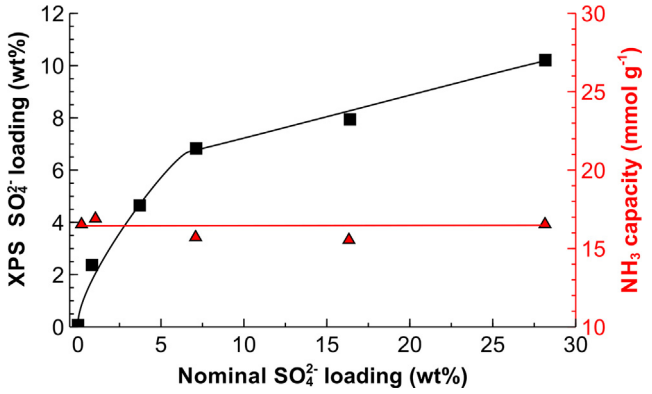

Fig. 12. SO_4^{2-} surface loading (left y-axis) and total NH_3 chemisorption capacity (right y-axis) as a function of nominal composition in the T1S catalysts.

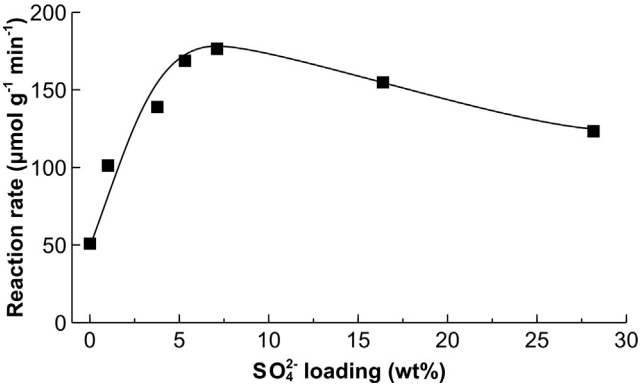

Fig. 14. Reaction rate between 4-phenylbutyric acid and aniline as a function of the SO_4^{2-} loading in a stirred tank reactor. Reaction conditions: 100 mL p-xylene solution of 4-phenylbutyric acid (50 mM) and aniline (50 mM), 320 mg sulfated catalyst, 6 bar(g), 200 °C.

From the pyridine adsorption and ammonia chemisorption experiments, it can be concluded that the sulfation treatment does not change the total number of the Lewis acid sites, but significantly increases their strength. As a result, the reaction rate demonstrates a classical volcano curve of catalytic activity with a maximum at a 7.5 wt% sulfur loading (Fig. 14). It is likely that at the lower loadings, the reaction rate is reduced due to a decreased catalyst coverage with the reactants, while at the higher loadings the reaction rate is reduced due to strong product adsorption (product inhibition). The optimum titania loading was chosen for the follow-up study with the T2 and T3 composite magnetic catalysts.

3.3. Sulfation of the composite catalysts

Two sulfation methods have been compared. In the first method, the as-synthesized T2A and T3A catalysts were sulfated following the approach already optimized for the T1 catalysts as discussed in the previous section. In the second method, the corresponding calcined catalysts (T2 and T3) were sulfated. The elemental analysis data (Table 2) show that both methods result in a slight decrease of titania loading likely due to its partial redispersion in the acidic solution.

The first method increases the surface area of sulfated catalysts by 13 and 46%, respectively, as compared to the corresponding T2 and T3 catalysts. On the contrary, the surface area of the T2S2 and T3S2 catalysts, prepared by the second method, decreased by 17 and 30%, respectively. This is caused by sintering of porous titania layer after the second calcination step (Table 2).

The SAR values of the catalysts obtained by the first method were lower as compared to the corresponding unsulfated catalysts (Table 2). This can be explained by a partial dissolution of nickel ferrite core in a sulfuric acid solution at a pH below 2 [66]. In contrast, the catalysts prepared by the second method showed higher SAR values as compared to the corresponding unsulfated catalysts. The SAR value increases due to higher coercivity of nickel ferrite nanoparticles with a mean size close to the transition region between single domain and multidomain structures [32]. It can be concluded that the intermediate silica shell protects the magnetic core from dissolution as the SAR value of T3S2 is considerably higher than that of T2S2 catalyst.

The rates for the reaction between 4-pheylbutyric acid and aniline over the sulfated composite catalysts are listed in Table 2. In line with the data obtained over T1 catalysts (Fig. 14), the reaction rates increased over the T3S2 and T3S1 sulfated catalysts by 30% and 80%, respectively, as compared to the corresponding unsulfated catalysts.. While the sulfation increased the reaction rate over the T1S catalyst by a factor of 3.5 (compared to T1), the observed enhancement over the composite catalysts was lower due to a lower titania loading. It should be noted that the effect over the T2 sulfated catalyst is less pronounced. This can be explained by the negative influence of the magnetic core on the titania shell as discussed above. The activity increases by 1.5 times after the sulfation treatment. The second calcination step then reduces the rate enhancement factor to 1.2 in the T2S2 catalyst.

Table 2
Specific surface area (S_{BET}), specific absorption rate (SAR), elemental analysis and catalytic activity data for the catalysts studied.

	S_{BET} ($m^2\ g^{-1}$)	SAR ($W\ g^{-1}$)	TiO_2 (wt%)	SiO_2 (wt%)	Reaction rate ($\mu mol\ g_{TiO2}^{-1}\ s^{-1}$)
T2S2	42.9	0.6	26	0	0.18
T2S1	58.7	0.8	25	0	0.22
T2	49.0	0.9	32	0	0.15
T3S2	33.8	0.6	16	12	0.28
T3S1	71.7	1.1	14	9	0.37
T3	52.0	1.5	17	13	0.21

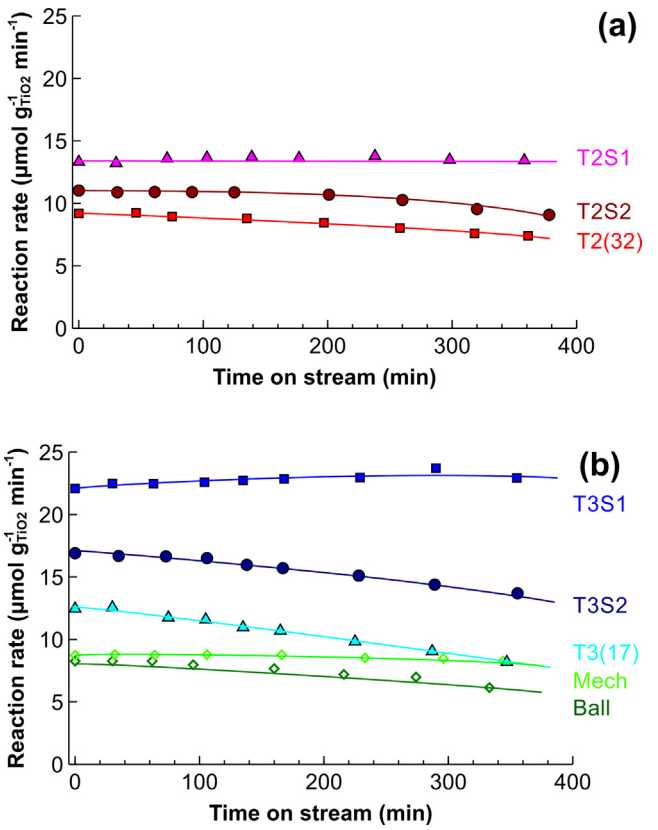

Fig. 15. Specific reaction rate as a function of time on stream over (a) core-shell and (b) core double shell catalysts as well as mechanical and ball-milled mixtures of the catalyst components. Reaction conditions: flow rate of 40 μL min^{-1} (50 mM 4-phenylbutyric acid, 50 mM aniline), 320 mg of the catalyst, 150 °C, 7 bar(g) in the RF-heated reactor.

The comparison of catalyst performance is presented in Fig. 15. No deactivation for 400 min on stream was observed over both T2S1 and T3S1 catalysts. However, the rate of deactivation over T2S2 and T3S2 catalysts was rather high and similar to that over the corresponding non-sulfated catalysts. This effect can be associated with the reduced rate of coke formation because the T2S1 and T3S1 catalysts have no Brønsted acid sites. A partial collapse of porous structure, as indicated by the reduced surface area (Table 2), always results in the formation of new Brønsted acid sites in the porous framework [47]. Likely, these sites are responsible for coking and therefore much higher deactivation rates are observed over these samples.

The comparison of reaction rates between the T3S1 composite catalyst, ball milled catalyst and the mechanical mixture of the same composition shows a notable difference (Fig. 15b). Over the ball-milled catalyst, the initial reaction rate was 2.5 times lower as compared to T3S1. In addition, a much faster deactivation kinetics was observed over the ball-milled catalyst. Over the mechanical mixture, the initial rate decreased by 1.7 times, without major changes in the deactivation kinetics. The decreased reaction rates in mixtures indicate that the close contact between the magnetic core and the shell in the ball-milled catalysts results in decreased reaction rates and faster deactivation. This effect is reduced in the mechanical mixture and completely eliminated in the core-double shell catalysts.

Because the T3S1 catalyst showed the highest catalytic activity with no deactivation for 6 h on stream, a further deactivation study was performed, Fig. 16. The reaction rate gradually decreased by 43% after 55 h on stream. The spent catalyst was flushed with a 35 wt% H_2O_2 solution at 90 °C adapting the method reported for

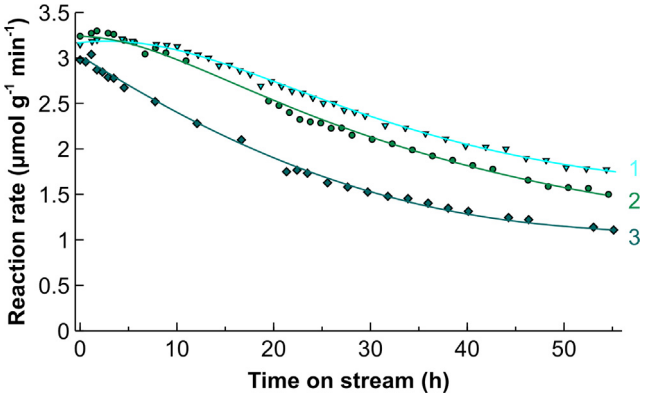

Fig. 16. Reaction rate as a function of time on stream catalyzed by the T3S1 catalyst over 2 regeneration cycles with H_2O_2. Reaction conditions: flow rate of 40 μL min^{-1} (50 mM 4-phenylbutyric acid, 50 mM aniline), 320 mg of the catalyst, 150 °C, 7 bar (g) in the RF-heated reactor.

batch recovery. The catalyst recovered showed the same initial activity as the fresh catalyst likely due to the complete coke removal [20]. However, after 9 h on stream, the regenerated catalyst demonstrated a faster deactivation rate compared to the fresh catalyst. As a result, the activity at the end of the second run was 14% lower compared to that observed after the first run. The catalyst activity after the second regeneration cycle was restored to 93% compared to the fresh catalyst and reached 32% of the initial activity for the fresh catalyst after the third run. Increasing deactivation rates suggest that H_2O_2 treatment removed light coke from the active sites, but that some coke remained resulting in the faster blockage of pores and a faster deactivation. Another possible reason is the negative effect of the hydrothermal regeneration treatment which could result in a partial collapse of the mesoporous network. However, the low amount of deactivated catalyst did not allow to perform a more detailed study.

The regeneration data show that the H_2O_2 treatment restores activity significantly. The integrated reaction rate (that is the total product output) for the second regeneration was only 28% lower compared to the fresh catalyst demonstrating good reusability and a long catalyst lifetime.

4. Conclusion

The performance of the core-shell (TiO_2@$NiFe_2O_4$) and core-double shell (TiO_2@SiO_2@$NiFe_2O_4$) composite magnetic catalysts was compared in the direct amide synthesis reaction between aniline and phenylbutyric acid in a flow reactor under radiofrequency heating at 300 kHz. Despite the similar magnetic core content, the double shell catalyst showed a 36% increase in specific heating rate compared to the core-shell catalyst. Due to the presence of an intermediate silica layer, the reaction rate normalized by weight of titania increased by 52% and the rate normalized by titania surface area increased by 61% compared to the core-shell catalyst. The data show that middle silica layer prevents the negative effect of interaction between the magnetic core and the titania shell and also increases the specific surface area of the catalyst layer.

The sulfation was optimised for titania catalysts containing only Lewis acid sites. The pyridine IR and ammonia chemisorption studies revealed that an increasing sulfate loading resulted in a higher acidity with the number of active sites being constant. The direct amide synthesis reaction rates, however, changed non-monotonously with the maximum at the sulfate loading of 7.5 wt% and the reaction rate 3.5 times higher compared to non-sulfated titania. The effect of sulfation demonstrates that the acidity of the catalysts for direct amide synthesis should be optimized to obtain the highest reaction rates.

Sulfation of the core-shell catalysts showed a further performance enhancement. The reaction rate over the double-shell TiO_2@SiO_2@$NiFe_2O_4$ catalyst was 1.7 times higher compared to the single-core shell TiO_2@$NiFe_2O_4$ catalyst and 2.5 times higher compared to mechanical mixtures of the catalyst constituents. Moreover, the deactivation rates were considerably lower over the sulfated core-double shell catalysts compared to single-shell and non-sulfated catalysts. The core-double shell catalysts also showed a high deactivation resistance working for more than 150 h with an overall activity decline of only 28% after two H_2O_2 regeneration cycles.

Acknowledgements

Financial support provided by the European Research Council (ERC) project 279867 and the Russian Science Foundation project 15-13-20015 is gratefully acknowledged.

Appendix A. Supplementary material

Supplementary data associated with this article can be found, in the online version, at http://dx.doi.org/10.1016/j.jcat.2017.09.010.

References

[1] C.O. Kappe, Controlled microwave heating in modern organic synthesis, Angew. Chem. Int. Ed. Engl. 43 (2004) 6250–6284, https://doi.org/10.1002/anie.200400655.
[2] P. Piyasena, C. Dussault, T. Koutchma, H.S. Ramaswamy, G.B. Awuah, Radio frequency heating of foods: principles, applications and related properties–a review, Crit. Rev. Food Sci. Nutr. 43 (2003) 587–606, https://doi.org/10.1080/10408690390251129.
[3] P. Lidström, J. Tierney, B. Wathey, J. Westman, Microwave assisted organic synthesis—a review, Tetrahedron 57 (2001) 9225–9283 (accessed May 9, 2013) http://www.sciencedirect.com/science/article/pii/S0040402001009061.
[4] F. Wiesbrock, R. Hoogenboom, U.S. Schubert, Microwave-assisted polymer synthesis: State-of-the-art and future perspectives, Macromol. Rapid Commun. 25 (2004) 1739–1764, https://doi.org/10.1002/marc.200400313.
[5] C. Oliver Kappe, Microwave dielectric heating in synthetic organic chemistry, Chem. Soc. Rev. 37 (2008) 1127–1139, https://doi.org/10.1039/b803001b.
[6] T.N. Glasnov, C.O. Kappe, Microwave-assisted synthesis under continuous-flow conditions, Macromol. Rapid Commun. 28 (2007) 395–410, https://doi.org/10.1002/marc.200600665.
[7] J.D. Moseley, P. Lenden, M. Lockwood, K. Ruda, J.P. Sherlock, A.D. Thomson, J.P. Gilday, A comparison of commercial microwave reactors for scale-up within process chemistry, Org. Process Res. Dev. 12 (2008) 30–40, https://doi.org/10.1021/op700186z.
[8] A. Díaz-Ortiz, A. de la Hoz, J. Alcázar, J.R. Carrillo, M. Antonia Herrero, A. Fontana, J. de Mata Muñoz, Reproducibility and scalability of solvent-free microwave-assisted reactions: from domestic ovens to controllable parallel applications, Comb. Chem. High Throughput Screen. 10 (2007) 163–169, https://doi.org/10.2174/138620707780126679.
[9] F. Benaskar, N.G.G. Patil, V. Engels, E.V.V. Rebrov, J. Meuldijk, L. a. A. Hulshof, V. Hessel, A.E.H.E.H. Wheatley, J.C.C. Schouten, Microwave-assisted Cu-catalyzed Ullmann ether synthesis in a continuous-flow milli-plant, Chem. Eng. J. 207–208 (2012) 426–439, https://doi.org/10.1016/j.cej.2012.06.147.
[10] I. Sharifi, H. Shokrollahi, S. Amiri, Ferrite-based magnetic nanofluids used in hyperthermia applications, J. Magn. Magn. Mater. 324 (2012) 903–915, https://doi.org/10.1016/j.jmmm.2011.10.017.
[11] A.E. Deatsch, B.A. Evans, Heating efficiency in magnetic nanoparticle hyperthermia, J. Magn. Magn. Mater. 354 (2014) 163–172, https://doi.org/10.1016/j.jmmm.2013.11.006.
[12] T.W.B. Riyadi, T. Zhang, D. Marchant, X. Zhu, Synthesis and fabrication of NiAl coatings with Ti underlayer using induction heating, Surf. Coatings Technol. 258 (2014) 154–159, https://doi.org/10.1016/j.surfcoat.2014.09.037.
[13] Z. Li, B. Zhao, P. Liu, B. Zhao, D. Chen, Y. Zhang, Synthesis of high-quality single-walled carbon nanotubes by high-frequency-induction heating, Phys. E Low-Dimensional Syst. Nanostructures. 40 (2008) 452–456, https://doi.org/10.1016/j.physe.2007.06.062.
[14] L. Wang, Y. Peng, X. Hu, X. Xu, Combustion synthesis of high purity SiC powder by radio-frequency heating, Ceram. Int. 39 (2013) 6867–6875, https://doi.org/10.1016/j.ceramint.2013.02.021.
[15] V. Rudnev, D. Loveless, R.L. Cook, M. Black, Handbook of Induction Heating, Marcel Dekker, New York. (2003) 796. http://www.asminternational.org/web/hts/home/-/journal_content/56/10192/75024G/PUBLICATION.

[16] S. Ceylan, C. Friese, C. Lammel, K. Mazac, A. Kirschning, Inductive heating for organic synthesis by using functionalized magnetic nanoparticles inside microreactors, Angew. Chemie - Int. Ed. 47 (2008) 8950–8953, https://doi.org/10.1002/anie.200801474.
[17] J. Hartwig, S. Ceylan, L. Kupracz, L. Coutable, A. Kirschning, Heating under high-frequency inductive conditions: Application to the continuous synthesis of the neurolepticum olanzapine (Zyprexa), Angew. Chemie - Int. Ed. 52 (2013) 9813–9817, https://doi.org/10.1002/anie.201302239.
[18] S.R. Chaudhuri, J. Hartwig, L. Kupracz, T. Kodanek, J. Wegner, A. Kirschning, Oxidations of allylic and benzylic alcohols under inductively-heated flow conditions with gold-doped superparamagnetic nanostructured particles as catalyst and oxygen as oxidant, Adv. Synth. Catal. 356 (2014) 3530–3538, https://doi.org/10.1002/adsc.201400261.
[19] M. Zhu, C. Wang, D. Meng, G. Diao, In situ synthesis of silver nanostructures on magnetic Fe3O4@C core-shell nanocomposites and their application in catalytic reduction reactions, J. Mater. Chem. A. 1 (2013) 2118–2125, https://doi.org/10.1039/C2TA00669C.
[20] Y. Liu, P. Gao, N. Cherkasov, E.V. Rebrov, Direct amide synthesis over core–shell TiO 2 @NiFe 2 O 4 catalysts in a continuous flow radiofrequency-heated reactor, RSC Adv. 6 (2016) 100997–101007, https://doi.org/10.1039/C6RA22659K.
[21] D. Beydoun, R. Amal, G. Low, S. McEvoy, Occurrence and prevention of photodissolution at the phase junction of magnetite and titanium dioxide, J. Mol. Catal. A Chem. 180 (2002) 193–200, https://doi.org/10.1016/S1381-1169(01)00429-0.
[22] B. Chang, Y. Tian, W. Shi, J. Liu, F. Xi, X. Dong, Magnetically separable porous carbon nanospheres as solid acid catalysts, RSC Adv. 3 (2013) 20999–21006, https://doi.org/10.1039/c3ra43208d.
[23] A.L. Costa, B. Ballarin, A. Spegni, F. Casoli, D. Gardini, Synthesis of nanostructured magnetic photocatalyst by colloidal approach and spray-drying technique, J. Colloid Interface Sci. 388 (2012) 31–39, https://doi.org/10.1016/j.jcis.2012.07.077.
[24] R.M. De Figueiredo, J.S. Suppo, J.M. Campagne, Nonclassical routes for amide bond formation, Chem. Rev. 116 (2016) 12029–12122, https://doi.org/10.1021/acs.chemrev.6b00237.
[25] A. El-Faham, F. Albericio, Peptide coupling reagents, more than a letter soup, Chem. Rev. 111 (2011) 6557–6602, https://doi.org/10.1021/cr100048w.
[26] M.M. Joullié, K.M. Lassen, Evolution of amide bond formation, Ark. Online J. Org. Chem. 2010 (2010) 189–250, https://doi.org/10.3998/ark.5550190.0011.816.
[27] C.A.G.N. Montalbetti, V. Falque, Amide bond formation and peptide coupling, Tetrahedron 61 (2005) 10827–10852, https://doi.org/10.1016/j.tet.2005.08.031.
[28] S. Nagarajan, P. Ran, P. Shanmugavelan, M. Sathishkumar, A. Ponnuswamy, K. Suk, Nahm, G. Gnana kumar, The catalytic activity of titania nanostructures in the synthesis of amides under solvent-free conditions, New J. Chem. 36 (2012) 1312–1319, https://doi.org/10.1039/c2nj40119c.
[29] T.K. Houlding, K. Tchabanenko, M.T. Rahman, E.V. Rebrov, Direct amide formation using radiofrequency heating, Org. Biomol. Chem. 11 (2013) 4171–4177, https://doi.org/10.1039/c2ob26930a.
[30] P.S. Chaudhari, S.D. Salim, R.V. Sawant, K.G. Akamanchi, Sulfated tungstate: a new solid heterogeneous catalyst for amide synthesis, Green Chem. 12 (2010) 1707–1710, https://doi.org/10.1039/c0gc00053a.
[31] F. Arena, C. Deiana, A.F. Lombardo, P. Ivanchenko, Y. Sakhno, G. Trunfio, G. Martra, Activity patterns of metal oxide catalysts in the synthesis of N-phenylpropionamide from propanoic acid and aniline, Catal. Sci. Technol. 5 (2015) 1911–1918, https://doi.org/10.1039/c4cy01504e.
[32] P. Gao, X. Hua, V. Degirmenci, D. Rooney, M. Khraisheh, R. Pollard, R.M. Bowman, E.V. Rebrov, Structural and magnetic properties of Ni1−xZnxFe2O4 (x=0, 0.5 and 1) nanopowders prepared by sol–gel method, J. Magn. Magn. Mater. 348 (2013) 44–50, https://doi.org/10.1016/j.jmmm.2013.07.060.
[33] T.K. Houlding, P. Gao, V. Degirmenci, K. Tchabanenko, E.V. Rebrov, Mechanochemical synthesis of TiO2/NiFe2O4 magnetic catalysts for operation under RF field, Mater. Sci. Eng. B Solid-State Mater. Adv. Technol. 193 (2015) 175–180, https://doi.org/10.1016/j.mseb.2014.12.011.
[34] O. Vaittinen, M. Metsälä, S. Persijn, M. Vainio, L. Halonen, Adsorption of ammonia on treated stainless steel and polymer surfaces, Appl. Phys. B. 115 (2013) 185–196, https://doi.org/10.1007/s00340-013-5590-3.
[35] M.A. Vannice, Kinetics of Catalytic Reactions, Springer Science+Business Media, New York (2005), https://doi.org/10.1007/b136380.
[36] N.B. Cherkasov, S.V. Savilov, A.S. Ivanov, V.V. Lunin, Bomb calorimetry as a bulk characterization tool for carbon nanostructures, Carbon NY 63 (2013) 324–329, https://doi.org/10.1016/j.carbon.2013.06.085.
[37] N. Cherkasov, S.V. Savilov, A.S. Ivanov, A.V. Egorov, V.V. Lunin, A.O. Ibhadon, Template synthesis and characterization of carbon nanomaterials from ferrocene crystals, Appl. Surf. Sci. 308 (2014) 388–395, https://doi.org/10.1016/j.apsusc.2014.04.181.
[38] S. Savilov, N. Cherkasov, M. Kirikova, A. Ivanov, V. Lunin, Multiwalled carbon nanotubes and nanofibers: similarities and differences from structural, electronic and chemical concepts; chemical modification for new materials design, Funct. Mater. Lett. 3 (2010) 289–294, https://doi.org/10.1142/S1793604710001421.
[39] A.E. Paladino, Phase equilibria in the ferrite region of the system Fe-Ni-O, J. Am. Ceram. Soc. 42 (1959) 168–175, https://doi.org/10.1111/j.1151-2916.1959.tb12941.x.
[40] J.M. Wesselinowa, Size and anisotropy effects on magnetic properties of antiferromagnetic nanoparticles, J. Magn. Magn. Mater. 322 (2010) 234–237, https://doi.org/10.1016/j.jmmm.2009.08.045.
[41] A. Hutlova, D. Niznansky, J.L. Rehspringer, C. Estournès, M. Kurmoo, High Coercive Field for Nanoparticles of CoFe2O4 in Amorphous Silica Sol-Gel, Adv. Mater. 15 (2003) 1622–1625, https://doi.org/10.1002/adma.200305305.
[42] V.K. Sharma, A. Baiker, Superparamagnetic effects in the ferromagnetic resonance of silica supported nickel particles, J. Chem. Phys. 75 (1981) 5596–5601, https://doi.org/10.1063/1.441997.
[43] C. De Julián Fernández, G. Mattei, C. Maurizio, E. Cattaruzza, S. Padovani, G. Battaglin, F. Gonella, F. D'Acapito, P. Mazzoldi, Magnetic properties of Co-Cu nanoparticles dispersed in silica matrix, J. Magn. Magn. Mater. 290 (2005) 187–190, https://doi.org/10.1016/j.jmmm.2004.11.178.
[44] J. Zhou, G. Zhao, X. Ren, B. Song, G. Han, Effects of diethanolamine on the evolution of silver/titanium dioxide sol–gel process, J. Sol-Gel Sci. Technol. 58 (2011) 148–155, https://doi.org/10.1007/s10971-010-2369-4.
[45] D. Fattakhova-Rohlfing, A. Zaleska, T. Bein, Three-dimensional titanium dioxide nanomaterials, Chem. Rev. 114 (2014) 9487–9558, https://doi.org/10.1021/cr500201c.
[46] L.M. Nikolić, L. Radonjić, V.V. Srdić, Effect of substrate type on nanostructured titania sol-gel coatings for sensors applications, Ceram. Int. 31 (2005) 261–266, https://doi.org/10.1016/j.ceramint.2004.05.012.
[47] H. Lundberg, F. Tinnis, N. Selander, H. Adolfsson, Catalytic amide formation from non-activated carboxylic acids and amines, Chem. Soc. Rev. 43 (2014) 2714, https://doi.org/10.1039/c3cs60345h.
[48] C. Deiana, Y. Sakhno, M. Fabbiani, M. Pazzi, M. Vincenti, G. Martra, Direct synthesis of amides from carboxylic acids and amines by using heterogeneous catalysts: evidence of surface carboxylates as activated electrophilic species, ChemCatChem. 5 (2013) 2832–2834, https://doi.org/10.1002/cctc.201300164.
[49] M. Hosseini-Sarvari, E. Sodagar, M.M. Doroodmand, Nano sulfated titania as solid acid catalyst in direct synthesis of fatty acid amides, J. Org. Chem. 76 (2011) 2853–2859, https://doi.org/10.1021/jo2002769.
[50] E. Barraud, F. Bosc, D. Edwards, N. Keller, V. Keller, Gas phase photocatalytic removal of toluene effluents on sulfated titania, J. Catal. 235 (2005) 318–326, https://doi.org/10.1016/j.jcat.2005.08.017.
[51] Y.A. Chesalov, G.B. Chernobay, T.V. Andrushkevich, FTIR study of the surface complexes of β-picoline, 3-pyridine-carbaldehyde and nicotinic acid on sulfated TiO2 (anatase), J. Mol. Catal. A Chem. 373 (2013) 96–107, https://doi.org/10.1016/j.molcata.2013.03.007.
[52] H. Zhao, P. Jiang, Y. Dong, M. Huang, B. Liu, A high-surface-area mesoporous sulfated nano-titania solid superacid catalyst with exposed (101) facets for esterification: facile preparation and catalytic performance, New J. Chem. 38 (2014) 4541–4548, https://doi.org/10.1039/C4NJ00494A.
[53] L.G. Devi, R. Kavitha, Enhanced photocatalytic activity of sulfur doped TiO2 for the decomposition of phenol: a new insight into the bulk and surface modification, Mater. Chem. Phys. 143 (2014) 1300–1308, https://doi.org/10.1016/j.matchemphys.2013.11.038.
[54] P. Goswami, J.N. Ganguli, C. Sao'an, Z. Jianqing, C. Chunan, J. Zhao, R. Xu, A novel synthetic approach for the preparation of sulfated titania with enhanced photocatalytic activity, RSC Adv. 3 (2013) 8878, https://doi.org/10.1039/c3ra23451g.
[55] K.J.A. Raj, B. Viswanathan, Single-step synthesis and structural study of mesoporous sulfated titania nanopowder by a controlled hydrolysis process, ACS Appl. Mater. Interfaces. 1 (2009) 2462–2469, https://doi.org/10.1021/am900437u.
[56] J. Zhong, J. Li, J. Zeng, S. Huang, W. Hu, J. Chen, M. Li, J. Wang, S. Zhang, Enhanced photo catalytic activity of sulfated silica-titania composites prepared by impregnation using using ammonium persulfate solution, Mater. Sci. Semicond. Process. 26 (2014) 62–68, https://doi.org/10.1016/j.mssp.2014.04.008.
[57] R.M. de Almeida, L.K. Noda, N.S. Gonçalves, S.M.P. Meneghetti, M.R. Meneghetti, Transesterification reaction of vegetable oils, using superacid sulfated TiO2-base catalysts, Appl. Catal. A Gen. 347 (2008) 100–105, https://doi.org/10.1016/j.apcata.2008.06.006.
[58] S. Yamazaki, K. Ichikawa, A. Saeki, T. Tanimura, K. Adachi, Photocatalytic degradation of chlorinated ethanes in the gas phase on the porous TiO2 pellets: effect of surface acidity, J. Phys. Chem. A. 114 (2010) 5092–5098, https://doi.org/10.1021/jp911842t.
[59] J.L. Ropero-Vega, A. Aldana-Pérez, R. Gómez, M.E. Niño-Gómez, Sulfated titania [TiO2/SO42−]: a very active solid acid catalyst for the esterification of free fatty acids with ethanol, Appl. Catal. A Gen. 379 (2010) 24–29, https://doi.org/10.1016/j.apcata.2010.02.020.
[60] Y. Wang, Y. Gan, R. Whiting, G. Lu, Synthesis of sulfated titania supported on mesoporous silica using direct impregnation and its application in esterification of acetic acid and n-butanol, J. Solid State Chem. 182 (2009) 2530–2534, https://doi.org/10.1016/j.jssc.2009.07.003.
[61] J. Sun, K. Zhu, F. Gao, C. Wang, J. Liu, C.H.F. Peden, Y. Wang, Direct conversion of bio-ethanol to isobutene on nanosized Zn xZryOz mixed oxides with balanced acid – base sites, J. Am. Chem. Soc. 133 (2011) 11096–11099, https://doi.org/10.1021/ja204235v.
[62] M. Niwa, K. Suzuki, N. Katada, T. Kanougi, T. Atoguchi, Ammonia IRMS-TPD study on the distribution of acid sites in mordenite, J. Phys. Chem. B. 109 (2005) 18749–18757, https://doi.org/10.1021/jp051304g.
[63] N. Cherkasov, T. Vazhnova, D.B. Lukyanov, Quantitative infra-red studies of Brønsted acid sites in zeolites: case study of the zeolite mordenite, Vib. Spectrosc. 83 (2016) 170–179, https://doi.org/10.1016/j.vibspec.2016.02.002.

[64] C.U. Ingemar Odenbrand, J.G.M. Brandin, G. Busca, Surface acidity of silica-titania mixed oxides, J. Catal. 135 (1992) 505–517, https://doi.org/10.1016/0021-9517(92)90050-R.
[65] X. Wang, J.C. Yu, P. Liu, X. Wang, W. Su, X. Fu, Probing of photocatalytic surface sites on SO42−/TiO2 solid acids by in situ FT-IR spectroscopy and pyridine adsorption, J. Photochem. Photobiol. A Chem. 179 (2006) 339–347, https://doi.org/10.1016/j.jphotochem.2005.09.007.
[66] K. Shih, T. White, J.O. Leckie, Nickel stabilization efficiency of aluminate and ferrite spinels and their leaching behavior, Environ. Sci. Technol. 40 (2006) 5520–5526, https://doi.org/10.1021/es0601033.